Morpho-elasticity of intestinal villi

V. Balbi, P. Ciarletta*

Institut Jean le Rond d'Alembert, CNRS UMR 7190,

Université Pierre et Marie Curie - Paris 6,

4 place Jussieu, case 162, 75005 Paris, France

Abstract

Villi are ubiquitous structures in the intestine of all vertebrates, originating from the embryonic development of the epithelial mucosa. Their morphogenesis has similar stages in living organisms but different forming mechanisms. In this work we model the emergence of the bi-dimensional undulated patterns in the intestinal mucosa from which villi start to elongate. The embryonic mucosa is modeled as a growing thick-walled cylinder, and its mechanical behavior is described using an hyperelastic constitutive model, which also accounts for the anisotropic characteristics of the reinforcing fibers at the *microstructural* level. The occurrence of surface undulations is investigated using a linear stability analysis based on the theory of incremental deformations superimposed on a finite deformation. The Stroh formulation of the incremental boundary value problem is derived and a numerical solution procedure is implemented for calculating the growth thresholds of instability. The numerical results are finally discussed with respect to different growth and materials properties.

In conclusion, we demonstrate that the emergence of intestinal villi in embryos is triggered by a differential growth between the mucosa and the mesenchymal tissues. The proposed model quantifies how both the geometrical and the mechanical properties of the mucosa drive the formation of previllous structures in embryos.

*Corresponding author. E-mail: pasquale.ciarletta@upmc.fr

1 Introduction

The inner surface of the intestinal tissue is covered by a columnar epithelium exhibiting invaginations, known as the crypts of Lieberkuhn, and finger-like projections, called villi [1]. Intestinal villi contain the majority of differentiated absorptive cells, possessing a peculiar morphology which allows to increase the surface area of the intestine as well as its capacity to absorb liquids and nutrients from food. In fact, an increased surface area decreases the average distance traveled by nutrient molecules, thus improving the effectiveness of the diffusion process. Villi are ubiquitous in the intestine of all vertebrates and their morphogenesis follows similar processes in all the organisms. In fact, villi originate from the embryonic development of a soft tissue, the mucosa, that cover the most internal part of organs and cavities exposed to an external environment, as airways, urogenital and gastrointestinal tract. The mucosa is made of three layers: the epithelium, the lamina propria and the muscularis mucosae, as depicted in Figure 1. Epithelial cells constitute the epithelial layer and cover the external part of the mucosa. The lamina

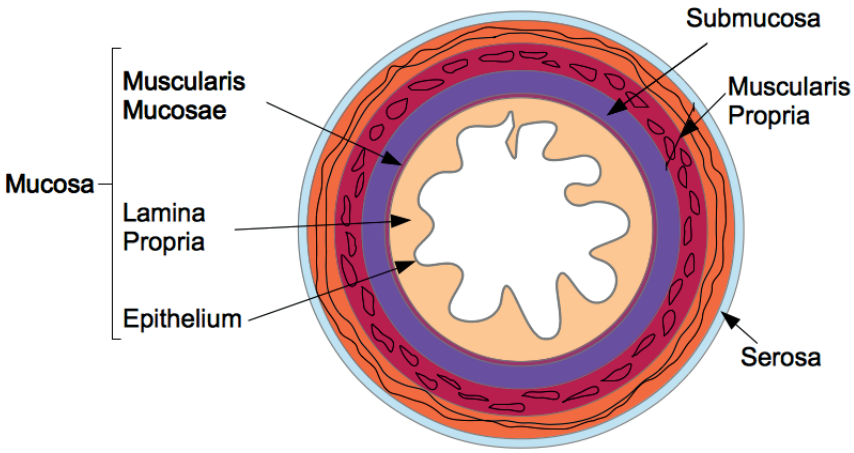

Figure 1: Schematic structure of the intestinal wall: the inner layer called mucosa (in which concur the epithelium, the lamina propria and the muscularis mucosae), the submucosa (made of dense irregular connective tissue), the muscularis propria (oriented smooth muscles) and the outer serosa layer are evidenced.

propria is the layer which is most specific to the anatomical origin. In particular, the lamina propria of the intestinal mucosa includes blood-vessels, lymph nodes and connective tissue composed by cells and an extracellular matrix made of ground substances (fluids) and fibers (collagen and elastin). Finally, the

lamina muscularis mucosae is a continuous thin sheet of smooth muscle cells.

The morphogenetic processes leading to the formation of the intestinal villi have been experimentally studied in various living organisms, highlighting similar development stages but different initiation mechanisms. In general, three formation stages have been identified: elevation of previllous ridges, delineation of villus bases and outgrowth of the definitive villi [2]. In human embryos, the formation of villi follows the development of mucosal structures which are characteristic of the anatomical origin of the tissue. In the upper part of the duodenum invaginations are observed during the mucosa growth, in the remainder of the duodenum vacuoles are present, villi are first seen as separate thickening of the mucosa in the upper part of the ileum whilst they are preceded by circumferential folding in its lower part [3]. In chick embryo samples [4,5] the formation of previllous ridges starts with the delineation of circumferential folds followed by a longitudinal zigzag patterns, emerging on the mucosal wall around 11-15 days after incubation, [6]. Between 14-17 days, the base of each villus starts to broaden, showing a transition from a zig-zag to a regular bi-dimensional undulation pattern which form the base structure for villi development. In fact, a cell population starts growing on each crest of the undulated pattern. The mature villi emerge from the elongation process before 25 days after incubation, forming the regular pattern shown in Figure 2.

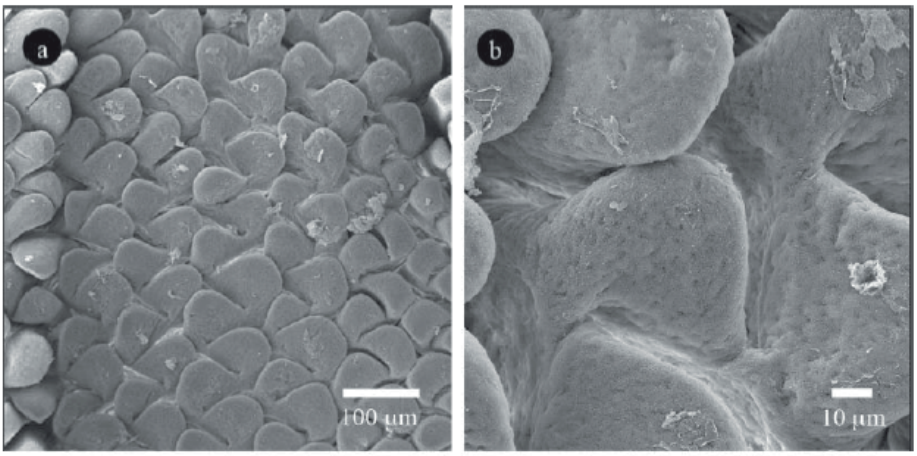

Figure 2: Scanning electron micrographs of emerging villi in the jejunum of turkey embryos (*reprinted with permission from* [4]). The micrographs are taken at 21 days of incubations, and shown using scales of 100μm (a) and 10μm (b) for outlining of the morphology of the bi-dimensional undulated pattern at the free surface of the mucosa.

During this morphogenetic process, the growing mucosa is geometrically confined by its surrounding tissues, the muscularis propria and the serosa. It is well established in morpho-elastic theories that geometrical incompatibilities during growth can give rise to residual stresses [7–9]. A number of morpho-

elastic models have been proposed to study the mechanical and geometrical aspects of circumferential buckling in tubular organs, considered as isotropic hyperelastic tissues [10–14]. Only recently Ciarletta and Ben Amar proposed a variational method for studying the segmentation instability in intestinal tissues accounting also for the anisotropic distribution of collagen fibers inside the tissue [15]. Anyway, none of these models considered the simultaneous occurrence of circumferential and longitudinal instabilities.
In this work, we aim at modelling the formation of the bi-dimensional undulated patterns in the embryonic intestinal mucosa, which characterize the initial stage of villi morphogenesis. In Section 2, we give a geometrical description of the model, using the multiplicative decomposition of the deformation gradient for describing the volumetric growth of the elastic mucosa. The mechanical behavior of the mucosa will be defined by the hyperelastic constitutive equations presented in Section 3, where the anisotropy of the tissue is accounted in terms of the stiffness and the orientation of the collagen fibers distributed under the epithelial layer. In Section 4, we will derive the equilibrium equations for the basic axial-symmetric solution and we perform a linear stability analysis for studying the emergence of the bi-dimensional patterns. The Stroh formulation of the incremental elastic equations will be given and the boundary value problem will be solved using a particular numerical scheme. Results relative to different growth and materials properties will be presented in Section 5, paying attention to the links between elastic parameters, growth and instability thresholds.

2 Definition of the geometrical model

In the following, we refer to (R, Θ, Z) as the cylindrical coordinates in the configuration $\mathcal{B}_0$, with orthonormal basis vectors $(\mathbf{E}_R, \mathbf{E}_\Theta, \mathbf{E}_Z)$ and to (r, θ, z) as the cylindrical coordinates in the actual configuration $\mathcal{B}_a$, with orthonormal *basis vectors* $(\mathbf{e}_r, \mathbf{e}_\theta, \mathbf{e}_z)$. The mucosa is described as a thick-walled tube, as sketched in Figure 3, whose geometry in the fixed reference configuration $\mathcal{B}_0$ is defined by

$$R_i \leq R \leq R_0, \quad 0 \leq \Theta \leq 2\pi, \quad 0 \leq Z \leq L, \tag{1}$$

where R_i and R_0 are the internal and external radii, respectively, and $L \gg R_0$ is the axial length of the cylinder. The morpho-elastic deformation is identified by the mapping χ, defined as:

$$\mathbf{x} = \chi(\mathbf{X}), \qquad \chi : \mathcal{B}_0 \to \mathcal{B}_a \tag{2}$$

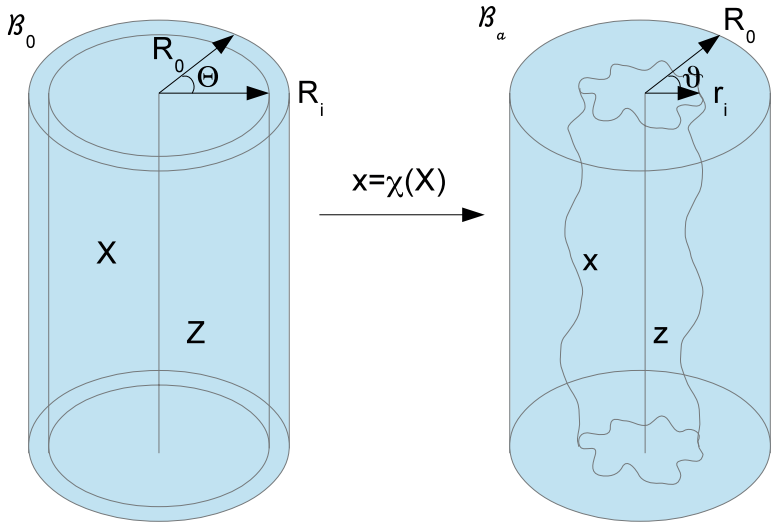

Figure 3: Geometrical model of the mucosa growth process: the mapping χ transforms the position $\mathbf{X}$ in the reference configuration $\mathcal{B}_0$ into the position $\mathbf{x}$ in the actual configuration $\mathcal{B}_a$.

where $\mathbf{X}$, $\mathbf{x}$ are the position vectors in the reference and actual configurations $\mathcal{B}_0$ and $\mathcal{B}_a$, respectively. The external radius is fixed during the entire process ($r_0 = r(R_0) = R_0$), since the outer layers, in particular the muscularis propria and the serosa, are much stiffer than the mucosa and can be considered a rigid constraint during mucosal growth. Moreover the free annular surfaces cannot slide longitudinally and the mucosal internal surface is free of external traction, because the inner intestinal pressure in embryos is negligible. As proposed by Rodriguez et al. [16], the *geometric* deformation gradient $\mathbf{F} = \mathrm{Grad}\,\mathbf{x} = \dfrac{\partial \chi(\mathbf{X})}{\partial \mathbf{X}}$, associated to the volumetric growth of the mucosa, can be split into two components, as follows:

$$\mathbf{F} = \mathbf{F}_e \mathbf{F}_g. \tag{3}$$

where $\mathbf{F}_g$ represents to the pure volumetric growth and $\mathbf{F}_e$ is the elastic deformation tensor. *The growth tensor represents a linear map of the tangent space and defines a natural grown state, which is not a configuration because the geometry of the tissue is not necessarily compatible with the constraint, as depicted in Figure 4.* The elastic deformation restores the compatibility of the tissue deformation, whilst residual stresses arise. For the sake of simplicity, we consider an homogeneous growth tensor in the form:

$$\mathbf{F}_g = diag(g_r, g_r, g_z) \qquad \text{with} \qquad J_g = \det \mathbf{F}_g = g_r^2 g_z \tag{4}$$

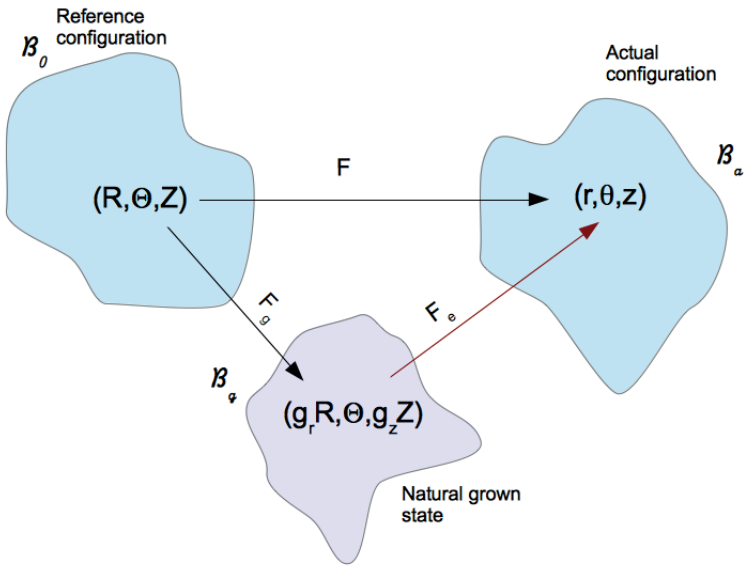

Figure 4: The multiplicative decomposition of the deformation gradient $\mathbf{F}$: the growth component $\mathbf{F}_g$ defines a natural grown state $\mathcal{B}_g$ in which geometrical incompatibilities are allowed, and the elastic component $\mathbf{F}_e$ restores the compatibility of the tissue deformation.

where the operator *diag* indicates that the growth tensor is diagonal. The growth rates in the radial and longitudinal directions are expresses as g_r and g_z, respectively, and they are assumed constant and positive definite. Finally, since the cells and extra-cellular matrix constituting the mucosa are prevalently composed by water, the tissue can be considered incompressible. Such an incompressibility constraint reads:

$$\det \mathbf{F}_e = 1. \tag{5}$$

In the next section, we introduce the non-linear constitutive equations of the material based on the microstructural properties of the mucosal layer.

3 Constitutive equations

Recalling that the characteristic viscoelastic time of soft tissues (seconds) is much smaller than their characteristic time of growth (days), we consider the mucosa having a hyperelastic behavior, so that a strain energy density function can be defined. The mucosa is modeled as a one-layered, homogeneous, incompressible tissue, composed by a cross-ply continuous distribution of collagen and elastin fibers

(anisotropic component), immersed into a homogeneous ground substance (isotropic component). We assume that collagen and fibers are distributed along the two principal directions m_α and $m_{-\alpha}$, defined as:

$$\begin{aligned}\mathbf{m}_\alpha &= (\sin\alpha)\mathbf{e}_\theta + (\cos\alpha)\mathbf{e}_z \\ \mathbf{m}_{-\alpha} &= -(\sin\alpha)\mathbf{e}_\theta + (\cos\alpha)\mathbf{e}_z\end{aligned} \tag{6}$$

where α is the cross-ply fiber angle *with respect to* the longitudinal direction $\mathbf{e}_z$. Hence, neglecting the mutual interaction between fibers and ground substance, we can use the additive decomposition proposed by Holzapfel and Ogden [17] and we can express the strain energy function as a sum of two terms:

$$\Psi(\mathbf{C}_e, \mathbf{m}_{\pm\alpha}) = \Psi_{Iso}(\mathbf{C}_e) + \Psi_{Aniso}(\mathbf{C}_e, \mathbf{m}_{\pm\alpha}) - p(\det\mathbf{C}_e - 1) \tag{7}$$

where Ψ_{Iso} is the isotropic component, a scalar function of the right Cauchy-Green tensor $\mathbf{C}_e$, and Ψ_{Aniso} is the anisotropic component, which also depends on the orientation of the fibers through the vectors $\mathbf{m}_{\pm\alpha}$, and p is a Lagrange multiplier for enforcing incompressibility. Let us assume a Neo-Hookean behavior of the ground substance, so that the isotropic contribution $\Psi_{Iso}(\mathbf{C}_e)$ in Eq. (7) reads:

$$\Psi_{Iso}(\mathbf{C}_e) = \frac{\mu}{2}(I_1 - 3) = \frac{\mu}{2}(\lambda_r^2 + \lambda_\theta^2 + \lambda_z^2 - 3) \tag{8}$$

where μ is the shear modulus, λ_l are the principal stretches, with $l \in \{r, \theta, z\}$, and $I_1 = \mathrm{tr}[\mathbf{C}_e]$ is the first invariant of $\mathbf{C}_e$. Let us now define the structural tensors $\mathbf{M}_{\pm\alpha} = \mathbf{m}_{\pm\alpha} \otimes \mathbf{m}_{\pm\alpha}$, where the symbol $\otimes$ indicates the dyadic product between two vectors ($(\mathbf{a}\otimes\mathbf{b})_{kj} = a_k b_j$). The anisotropic strain energy function $\Psi_{Aniso}(\mathbf{C}_e, \mathbf{m}_{\pm\alpha})$ can be defined as [18]:

$$\Psi_{Aniso}(\mathbf{C}_e, \mathbf{m}_{\pm\alpha}) = k_1 I_4, \tag{9}$$

where k_1 is the anisotropic stiffness of the material, and I_4 is a structural pseudo-invariant, which reads:

$$\begin{aligned}I_4 &= \frac{1}{4}(\mathbf{C}_e + \mathbf{C}_e^{-1} - 2\mathbf{I}) : (\mathbf{M}_\alpha + \mathbf{M}_{-\alpha}) = \frac{1}{4}\left((\lambda_{+\alpha} - \lambda_{+\alpha}^{-1})^2 + (\lambda_{-\alpha} - \lambda_{-\alpha}^{-1})^2\right) \\ &= \frac{1}{2}\left[\left(\frac{1}{\lambda_z^2} + \lambda_z^2 - 2\right)\cos(\alpha)^2 + \left(\frac{1}{\lambda_\theta^2} + \lambda_\theta^2 - 2\right)\sin(\alpha)^2\right]\end{aligned} \tag{10}$$

where the symbol : indicates the so-called saturation operator between two tensors ($\mathbf{A} : \mathbf{B} = \mathrm{tr}[\mathbf{A}^T\mathbf{B}] = A_{kj}B_{kj}$, *and* $\lambda_{\pm\alpha} = |\boldsymbol{F}\boldsymbol{m}_{\pm\alpha}|$ *are the fiber stretches along the directions* $\pm\alpha$. We also note that the strain

energy in Eq. (9) is polyconvex and physically consistent both with the compression and the extension of fibers. From constitutive arguments, the nominal stress tensor $\mathbf{S}$ of the mucosa can be expressed as:

$$\mathbf{S} = 2\psi_1 \mathbf{F}_e^T + \sum_{j=\pm\alpha} \frac{1}{2}\psi_4 (\mathbf{m}_j \otimes \mathbf{m}_j)\mathbf{F}_e^T - \sum_{j=\pm\alpha} \frac{1}{2}\psi_4 (\mathbf{C}_e^{-1}\mathbf{m}_j \otimes \mathbf{m}_j \mathbf{F}_e^{-1}) - p\mathbf{F}_e^{-1} \tag{11}$$

while the Cauchy stress tensor $\boldsymbol{\sigma}$ reads:

$$\boldsymbol{\sigma} = 2\psi_1 \mathbf{B}_e + \sum_{j=\pm\alpha} \frac{1}{2}\psi_4 (\mathbf{F}_e\mathbf{m}_j \otimes \mathbf{F}_e\mathbf{m}_j - \mathbf{F}_e^{-T}\mathbf{m}_j \otimes \mathbf{F}_e^{-T}\mathbf{m}_j) - p\mathbf{I} = \boldsymbol{\Sigma} - p\mathbf{I} \tag{12}$$

where $\psi_1 = \partial\Psi/\partial I_1$, $\psi_4 = \partial\Psi/\partial I_4$ and $\boldsymbol{\Sigma} = \mu\mathbf{B}_e + \sum_{j=\pm\alpha} \frac{1}{2} k_1 (\mathbf{F}_e\mathbf{m}_j \otimes \mathbf{F}_e\mathbf{m}_j - \mathbf{F}_e^{-T}\mathbf{m}_j \otimes \mathbf{F}_e^{-T}\mathbf{m}_j)$, with $\mathbf{B}_e$ indicating the left Cauchy-Green tensor. In absence of body forces, the equilibrium equations for the mucosa read:

$$\mathrm{Div}\,\mathbf{S} = 0, \quad \mathrm{div}\,\boldsymbol{\sigma} = 0 \tag{13}$$

where Div and div are the divergence operators in the reference and actual configurations, respectively. Finally, we can define the following boundary conditions:

$$\mathbf{S}^T \cdot \mathbf{N} = 0 \quad \text{on} \quad R = R_i, \qquad \boldsymbol{\sigma} \cdot \mathbf{n} = 0 \quad \text{on} \quad r = r_i \tag{14}$$

where $\mathbf{N}$ and $\mathbf{n}$ are the outer normal units in the reference and actual configurations, respectively. In the next section, we derive the basic axial-symmetric solution of Eqs.(13, 14) and we perform its linear stability analysis.

4 Axial-symmetric solution and linear stability analysis

Growth instabilities are usually investigated using the method of incremental deformations superposed on finite deformations. At the bottom of this method, the fundamental idea is to consider an infinitesimal perturbation of a basic elastic solution in order to perform a linear stability analysis. Let us first solve the equilibrium equations in Eqs.(13,14) for calculating the basic axial-symmetric solution of the associated boundary value problem (BVP), as well as the residual stress distribution inside the tissue. Second, we *define an* incremental deformation on the finite solution, and we perform a bifurcation analysis for solving the associated BVP and identifying the instability thresholds.

4.1 Basic axial-symmetric solution

Let us now derive the axial-symmetric solution for the growing mucosa, taking into account the residual stresses arising from the geometrical constraint. Considering the incompressibility constraint in Eq.(5), the spatial components of the axial-symmetric deformation read:

$$\begin{cases} r(R,\Theta,Z) = \sqrt{g_r^2 g_z R^2 + a} \\ \theta(R,\Theta,Z) = \Theta \\ z(R,\Theta,Z) = Z. \end{cases} \tag{15}$$

where $a = (1 - g_r^2 g_z) R_0^2$ is imposed by the geometrical constraint at R_0. According to Eq.(15), the principal stretches λ_r, λ_θ and λ_z are given by:

$$\lambda_r = \frac{r_{,R}}{g_r} \quad \lambda_\theta = \frac{r}{g_r R} \quad \lambda_z = \frac{1}{g_z}, \tag{16}$$

where the comma denotes the partial differentiation. Accordingly, the basic elastic deformation gradient $\mathbf{F}_e^{(0)}$ rewrites:

$$\mathbf{F}_e^{(0)} = diag(\lambda_r, \lambda_\theta, \lambda_z). \tag{17}$$

so that the left Cauchy-Green tensor $\mathbf{B}_e$ is defined as $\mathbf{B}_e = \mathbf{F}_e^{(0)} (\mathbf{F}_e^{(0)})^T = diag(\lambda_r^2, \lambda_\theta^2, \lambda_z^2)$. Since we are considering an incompressible, hyperelastic solid, the principal components of the Cauchy stress $\boldsymbol{\sigma}$ from Eq. (12) read:

$$\begin{aligned} \sigma_{rr}(r) &= \Sigma_r(r) - p(r) = \mu \lambda_r^2 - p(r) \\ \sigma_{\theta\theta}(r) &= \Sigma_\theta(r) - p(r) = \mu \lambda_\theta^2 + \frac{k1}{2} \left(\lambda_\theta^2 - \frac{1}{\lambda_\theta^2} \right) \sin^2(\alpha) - p(r) \\ \sigma_{zz}(r) &= \Sigma_z(r) - p(r) = \mu \lambda_z^2 + \frac{k1}{2} \left(\lambda_z^2 - \frac{1}{\lambda_z^2} \right) \cos^2(\alpha) - p(r) \end{aligned} \tag{18}$$

where Σ_k, $k = \{r, \theta, z\}$ are the diagonal components of $\boldsymbol{\Sigma}$ in Eq. (12). Considering the axial-symmetric solution in Eq. (15), the only non trivial equilibrium equation of Eq. (13) is given by:

$$\frac{d\sigma_{rr}(r)}{dr} + \frac{1}{r}(\sigma_{rr}(r) - \sigma_{\theta\theta}(r)) = 0 \tag{19}$$

and the only unknown is the *Lagrange* multiplier p. Imposing the boundary condition in Eq. (14), ensuring no stress on the internal surface, p can be obtained solving Eq. (19) as:

$$p(r) = \Sigma_r(r) + \int_{r_i}^{r} \frac{\Sigma_r(s) - \Sigma_\theta(s)}{s} ds \tag{20}$$

Substituting Eq.(20) in Eq.(18), we obtain the spatial distribution of the residual stresses inside the mucosa as a function of the growth rates. In the following, we will perform a linear stability analysis introducing an infinitesimal perturbation on the axial-symmetric solution.

4.2 Incremental deformation

Let us consider an infinitesimal perturbation of the basic grown position $\mathbf{x}^{(0)} = \chi^{(0)}(\mathbf{X})$, defined as:

$$\chi(\mathbf{X}) = \chi^{(0)}(\mathbf{X}) + \varepsilon\chi^{(1)}(\mathbf{x}^{(0)}) \tag{21}$$

where $|\varepsilon| \ll 1$, so that the term $\chi^{(1)}(\mathbf{x}^{(0)})$ can be regarded as a first-order incremental displacement with respect to the axial-symmetric configuration.
Considering the spatial displacement gradient $\mathbf{\Gamma} = \operatorname{grad}\chi^{(1)}(\mathbf{x}^{(0)})$ associated to the incremental deformation, the perturbed elastic deformation gradient reads:

$$\mathbf{F}_e = \mathbf{F}_e^{(0)} + \delta\mathbf{F}_e^{(0)} = \mathbf{F}_e^{(0)} + \varepsilon\mathbf{\Gamma}\mathbf{F}_e^{(0)} \tag{22}$$

where $\delta\mathbf{F}_e^{(0)}$ is the increment of the basic elastic deformation gradient $\mathbf{F}_e^{(0)}$, as depicted in Figure 5. Now, we want to rewrite the equilibrium equations in the perturbed configuration $\delta\mathcal{B}_a$. The nominal stress in Eq. (22) is given after perturbation by:

$$\mathbf{S} = \underbrace{\mathbf{S}^{(0)}}_{\text{zero-order term}} + \underbrace{\varepsilon\dot{\mathbf{S}}}_{\text{first-order term}} \tag{23}$$

where the zero-order term $\mathbf{S}^{(0)}$ is the nominal stress calculated for the axial-symmetric configuration. Let $\dot{\mathbf{S}}$ be the associated increment of the nominal stress tensor $\mathbf{S}$. By differentiating the constitutive equation in Eq. (11), it reads:

$$\dot{\mathbf{S}} = \mathcal{A}^1\delta\mathbf{F}_e^{(0)} + p(\mathbf{F}_e^{(0)})^{-1}\delta\mathbf{F}_e^{(0)}(\mathbf{F}_e^{(0)})^{-1} - q(\mathbf{F}_e^{(0)})^{-1}. \tag{24}$$

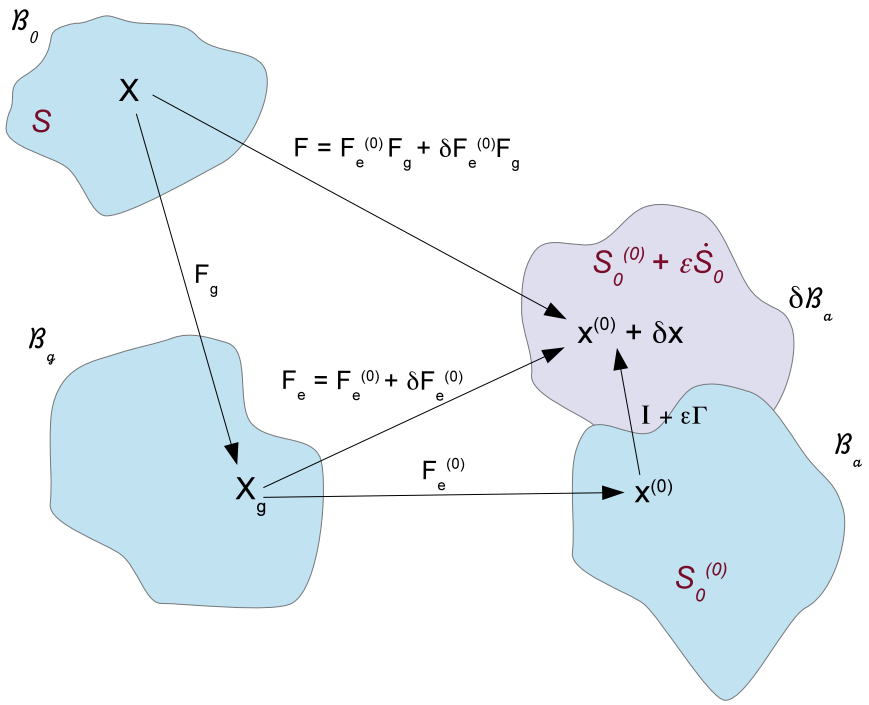

Figure 5: Scheme of the deformation gradient $\mathbf{F}$ and the elastic deformation gradient $\mathbf{F}_e$, after the introduction of the incremental displacement gradient $\mathbf{\Gamma}$. The term $\dot{\mathbf{S}}_0$ represents the projection of the incremental nominal stress in the perturbed configuration $\delta\mathcal{B}_a$.

In Eq. (24), the term $q = \dot{p}$ is the increment in p and $\mathcal{A}^1$ is the fourth-order tensor of the elastic moduli [19], defined as:

$$\mathcal{A}^1 = \frac{\partial \Psi}{\partial \mathbf{F}_e^{(0)} \partial \mathbf{F}_e^{(0)}}, \quad \mathcal{A}^1_{\gamma k \beta j} = \frac{\partial^2 \Psi}{\partial F^{(0)}_{k\gamma} \partial F^{(0)}_{j\beta}}. \tag{25}$$

Since the zero-order term in Eq. (23) satisfies the first of Eq. (13), the incremental equilibrium equations rewrite:

$$\mathrm{Div}\, \dot{\mathbf{S}} = 0. \tag{26}$$

Now, let us define the push-forward of $\dot{\mathbf{S}}$ in the perturbed configuration as:

$$\dot{\mathbf{S}}_0 = \mathbf{F}_e^{(0)} \dot{\mathbf{S}} = \mathcal{A}^1_0 \mathbf{\Gamma} + p\mathbf{\Gamma} - q\mathbf{I} \tag{27}$$

where $\mathcal{A}_0^1$ is the push-forward of $\mathcal{A}^1$, also known as the tensor of instantaneous moduli:

$$\mathcal{A}^1_{0hklj} = F^{(0)}_{h\gamma} F^{(0)}_{l\beta} \mathcal{A}^1_{\gamma k\beta j}. \tag{28}$$

From Eqs.(17, 28), the non-zero components of $\mathcal{A}_0^1$ are:

$$\begin{aligned}
&\mathcal{A}^1_{0kkjj} = \lambda_k \lambda_j \Psi_{kj} \\
&\mathcal{A}^1_{0kjkj} = (\lambda_k \Psi_k - \lambda_j \Psi_j) \frac{\lambda_k^2}{\lambda_k^2 - \lambda_j^2}, \quad k \neq j \\
&\mathcal{A}^1_{0kjjk} = \mathcal{A}^1_{0jkkj} = \mathcal{A}^1_{0kjkj} - \lambda_k \Psi_k, \quad k \neq j
\end{aligned} \tag{29}$$

where $\Psi_k = \partial \Psi / \partial \lambda_k$, $\Psi_{kj} = \partial^2 \Psi / \partial \lambda_k \partial \lambda_j$ and with k and j running over r, θ and z. Using the *well-known* properties of Piola transformations, the equilibrium equations in Eq. (26) can be written in the spatial form as:

$$\operatorname{div} \dot{\mathbf{S}}_0 = 0 \tag{30}$$

where $\dot{\mathbf{S}}_0$ is given by Eq. (27). Introducing the stress components in Eq. (30), we can obtain the three incremental equilibrium equations as:

$$\begin{aligned}
&\frac{\partial (r \dot{S}_{0rr})}{\partial r} + \frac{\partial \dot{S}_{0\theta r}}{\partial \theta} + r \frac{\partial \dot{S}_{0zr}}{\partial z} - \dot{S}_{0\theta\theta} = 0 \\
&\frac{\partial (r \dot{S}_{0r\theta})}{\partial r} + \frac{\partial \dot{S}_{0\theta\theta}}{\partial \theta} + r \frac{\partial \dot{S}_{0z\theta}}{\partial z} + \dot{S}_{0\theta r} = 0 \\
&\frac{\partial (r \dot{S}_{0rz})}{\partial r} + \frac{\partial \dot{S}_{0\theta z}}{\partial \theta} + r \frac{\partial \dot{S}_{0zz}}{\partial z} = 0
\end{aligned} \tag{31}$$

Let us now assume the incremental deformation in the following form: $\chi^{(1)}(\mathbf{x}^{(0)})$:

$$\chi^{(1)}(r, \theta, z) = u(r, \theta, z) \mathbf{e}_r + v(r, \theta, z) \mathbf{e}_\theta + w(r, \theta, z) \mathbf{e}_z \tag{32}$$

where (u, v, w) are scalar functions representing the incremental displacements. According to Eq. (32), the displacement gradient $\mathbf{\Gamma}$ reads:

$$\mathbf{\Gamma} = \begin{pmatrix} u_{,r} & (u_{,\theta} - v)/r & u_{,z} \\ v_{,r} & (u_{,\theta} + v)/r & v_{,z} \\ w_{,r} & (v_{,\theta})/r & w_{,z} \end{pmatrix}. \tag{33}$$

Since we are dealing with an incompressible tissue, the incremental incompressibility condition reads:

$$\operatorname{tr}\boldsymbol{\Gamma} = u_{,r} + \frac{u + v_{,\theta}}{r} + w_{,z} = 0. \tag{34}$$

Eqs. (31,34) define a system of four partial differential equations, where the four unknowns are the three incremental displacements in Eq. (32) and the increment q of the lagrange multiplier. Once derived the incremental equilibrium equations, we need to impose the necessary boundary conditions for solving the system of Eqs. (31,34) and defining an adjacent equilibrium to the axial-symmetric deformation.

4.3 Stroh formulation of the BVP and numerical solution

In order to solve Eqs. (31,34), we transform the system of partial differential equations into a system of ordinary differential equations of the first order. This strategy is also known as the Stroh formulation of the elastic problem [20]. First of all, let us consider incremental displacements in the form:

$$(u, v, w, q) = (U(r), V(r), W(r), Q(r))e^{i(m\theta + k_z z)} \tag{35}$$

where m (resp. $k_z = \frac{2n\pi}{L}$) is the circumferential (resp. longitudinal) mode of the perturbation, with m and n positive integers, and i is the imaginary unit. Using the perturbation defined in Eq. (35), the deformed mucosa is depicted in Figure 6, showing the characteristic bi-dimensional undulated pattern at the inner surface emerging at the initial stages of intestinal villi formation.
For physical compatibility, the incremental stress components have the similar form:

$$\dot{S}_{0kj} = S_{0kj}(r)e^{i(m\theta + k_z z)} \tag{36}$$

where S_{0kj} is a function of r, with indices $\{k, j\}$ running over $\{r, \theta, z\}$. Substituting Eqs. (29,35,36) in the incremental constitutive equations for $\dot{S}_{0rr}$, given by Eq. (27), we obtain:

$$Q = \left(\mathcal{A}^1_{0rrrr} + p\right) U' + \mathcal{A}^1_{0rr\theta\theta}\frac{imU + V}{r} + \mathcal{A}^1_{0rrzz} ik_z W - (S_{0rr}) \tag{37}$$

Similarly, from the constitutive equations for the incremental components $\dot{S}_{0r\theta}$ and $\dot{S}_{0rz}$, we can explicit

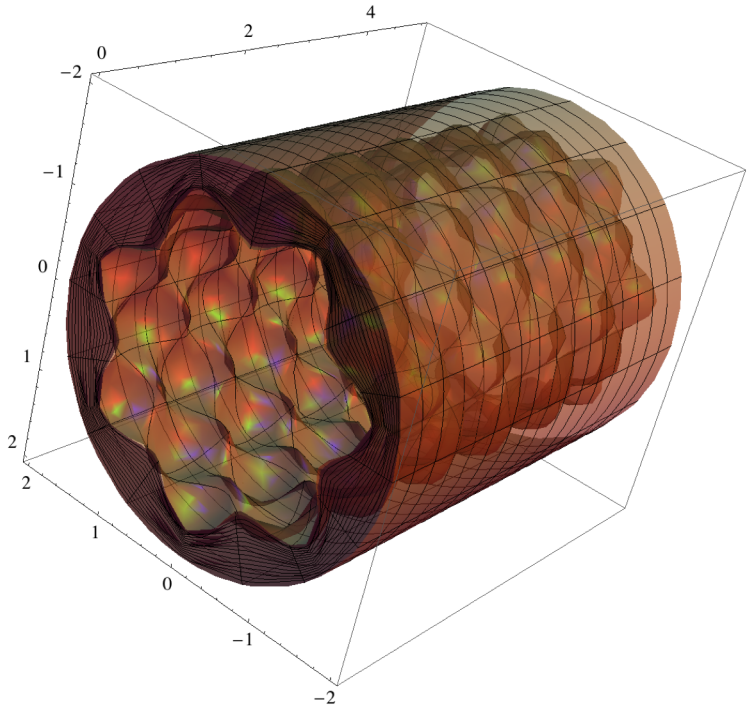

Figure 6: Morphology of the intestinal mucosa after imposing a perturbation of the axial-symmetric solution of the elastic problem, having the form of Eq. (35). The geometrical parameters are $r_0 = 2$, $r_i = 1.5$, $L = 5$, $m = 7$, $k_z = 5$ and $\epsilon = 0.15$.

V' and W' as:

$$V' = \frac{S_{0r\theta}}{\mathcal{A}^1_{0r\theta r\theta}} - \left(\mathcal{A}^1_{0r\theta\theta r} + p\right) \frac{imU - V}{r\mathcal{A}^1_{0r\theta r\theta}} \tag{38}$$

$$W' = \frac{S_{0rz}}{\mathcal{A}^1_{0rzrz}} - \frac{\left(\mathcal{A}^1_{0rzzr} + p\right) ik_z U}{\mathcal{A}^1_{0rzrz}}. \tag{39}$$

Furthermore, the incremental incompressibility condition in Eq. (34) yields:

$$U' = -\frac{U + imV}{r} - ik_z W. \tag{40}$$

Now, we first replace the components $\dot{S}_{0rr}, \dot{S}_{0r\theta}, \dot{S}_{0rz}$ in Eq. (31) using Eq. (36) and setting $s_{0kj} = (irS_{0kj})$ for $(k, j) = \{r, \theta, z\}$ [21]. Using Eqs. (27,29,35), the incremental equilibrium equations take the

following expressions:

$$\begin{aligned}&\frac{1}{ir}\left(s_{0rr}\right)'+m\frac{1}{r}\left(-\mathcal{A}^1_{0\theta r\theta r}\frac{mU+iV}{r}+i\left(\mathcal{A}^1_{0\theta rr\theta}+p\right)V'\right)+k_z^2\mathcal{A}^1_{0zrzr}U\\&+k_zi\left(\mathcal{A}^1_{0zrrz}+p\right)W'-\tfrac{1}{r}\left(\mathcal{A}^1_{0\theta\theta rr}U'+\mathcal{A}^1_{0\theta\theta\theta}\tfrac{miU+V}{r}+k_zi\mathcal{A}^1_{0\theta\theta zz}W+p\tfrac{miU+V}{r}-Q\right)=0\end{aligned}\tag{41}$$

$$\begin{aligned}&\frac{1}{ir}\left(s_{0r\theta}\right)'+\frac{m}{r}\left(i\mathcal{A}^1_{0\theta\theta rr}U'-\mathcal{A}^1_{0\theta\theta\theta}\frac{mU-iV}{r}-mk_z\mathcal{A}^1_{0\theta\theta zz}W-p\frac{mU-iV}{r}-iQ\right)\\&-k_z^2\mathcal{A}^1_{0z\theta z\theta}V-mk_z\mathcal{A}^1_{0z\theta\theta z}\tfrac{V}{r}-mk_z\tfrac{V}{r}p+\tfrac{1}{r}\left(\mathcal{A}^1_{0\theta rr\theta}V'+\mathcal{A}^1_{0\theta r\theta r}\tfrac{miU-V}{r}+pV'\right)=0\end{aligned}\tag{42}$$

$$\frac{1}{ri}\left(s_{0rz}\right)'-\frac{m}{r}\left(\frac{1}{r}\mathcal{A}^1_{0\theta z\theta z}+k_z\left(\mathcal{A}^1_{0\theta zz\theta}+p\right)\right)V+k_z\left(\mathcal{A}^1_{0zzrr}iU'-\mathcal{A}^1_{0zz\theta\theta}-k_z\left(\mathcal{A}^1_{0zzzz}+p\right)W-iQ\right)=0\tag{43}$$

where prime denotes the derivative respect to the variable r. Let us define the displacement-traction vector $\boldsymbol{\eta}$ as:

$$\boldsymbol{\eta}=\{U,V,W,s_{0rr},s_{0r\theta},s_{0rz}\}^T.\tag{44}$$

Substituting Eqs.(37-40) in Eqs.(41-43), we eliminate the unknown Q and we obtain three ordinary differential equations of first order that depend only on $(U,V,W,s_{0rr},s_{0r\theta},s_{0rz})$. Accordingly, Eqs. (38-43) can be written in a more compact formulation as follows:

$$\frac{d\boldsymbol{\eta}(\boldsymbol{r})}{dr}=\frac{i}{r}\mathbf{G}(r)\boldsymbol{\eta}(r),\tag{45}$$

where the Stroh matrix $\mathbf{G}$ has the form:

$$\mathbf{G}=\begin{pmatrix}\mathbf{G}_1 & \mathbf{G}_2\\ \mathbf{G}_3 & \mathbf{G}_4\end{pmatrix}.\tag{46}$$

In particular, the four blocks of $\mathbf{G}$ read:

$$\mathbf{G}_1=\begin{pmatrix}i & -m & -k_zr\\ -m(1-\sigma_1) & -i(1-\sigma_1) & 0\\ -k_zr(1-\sigma_2) & 0 & 0\end{pmatrix},\quad \mathbf{G}_2=\begin{pmatrix}0 & 0 & 0\\ 0 & -1/\alpha_1 & 0\\ 0 & 0 & -1/\alpha_2\end{pmatrix},\tag{47}$$

$$\mathbf{G}_3 = \begin{pmatrix} \kappa_{11} & i\kappa_{12} & i\kappa_{13} \\ -i\kappa_{12} & \kappa_{22} & \kappa_{23} \\ -i\kappa_{13} & \kappa_{23} & \kappa_{33} \end{pmatrix}, \quad \mathbf{G}_4 = \mathbf{G}_1^+ \tag{48}$$

where $\mathbf{G}_1^+$ is the adjugate (transpose conjugate) of $\mathbf{G}_1$ and

$$\begin{aligned}
\kappa_{11} &= m^2[\gamma_1 - \alpha_1(1-\sigma_1)^2] + k_z^2 r^2[\gamma_2 - \alpha_2(1-\sigma_2)^2] + 2[\beta_1 + \alpha_1(1-\sigma_1)] \\
\kappa_{12} &= m[2\beta_1 + \gamma_1 + \alpha_1(1-\sigma_1^2)] \\
\kappa_{13} &= k_z r[2\beta_2 + \alpha_3(1-\sigma_3)^2] \\
\kappa_{22} &= 2m^2[\beta_1 + \alpha_1(1-\sigma_1)] + \gamma_1 - \alpha_1(1-\sigma_1)^2 + k_z^2 r^2 \gamma_3 \\
\kappa_{23} &= 2mk_z r[\beta_2 + \alpha_3(1-\sigma_3)] \\
\kappa_{33} &= m^2\alpha_3 + 2k_z^2 r^2[\beta_3 + \alpha_2(1-\sigma_2)]
\end{aligned} \tag{49}$$

with:

$$\begin{aligned}
&\gamma_1 = A^1_{0\theta r\theta r}, \qquad \alpha_1 = \mathcal{A}^1_{0r\theta r\theta}, \qquad \sigma_1 = \sigma_{rr}/\alpha_1, \\
&\gamma_2 = A^1_{0zrzr}, \qquad \alpha_2 = \mathcal{A}^1_{0rzrz}, \qquad \sigma_2 = \sigma_{rr}/\alpha_2, \\
&\gamma_3 = A^1_{0z\theta z\theta}, \qquad \alpha_3 = \mathcal{A}^1_{0\theta z\theta z}, \qquad \sigma_3 = \sigma_{\theta\theta}/\alpha_3, \\
&2\beta_1 = A^1_{0rrrr} + A^1_{0\theta\theta\theta\theta} - 2A^1_{0rr\theta\theta} - 2A^1_{0r\theta\theta r}, \\
&2\beta_2 = A^1_{0rrrr} - A^1_{0rr\theta\theta} - A^1_{0rrzz} + A^1_{0\theta\theta zz} - A^1_{0z\theta\theta z}, \\
&2\beta_3 = A^1_{0rrrr} + A^1_{0zzzz} - 2A^1_{0rrzz} - 2A^1_{0rzzr}.
\end{aligned} \tag{50}$$

In order to solve Eq.(45), we must impose the boundary condition ensuring the vanishing of the perturbation at the external radius $r = R_0$, being:

$$U = V = W = 0 \quad \text{on} \quad r = R_0. \tag{51}$$

Finally, the stress-free boundary condition at the internal radius $r = r_i$ imposes:

$$s_{0rr} = s_{0r\theta} = s_{0rz} = 0 \quad \text{on} \quad r = r_i. \tag{52}$$

In the following, we will present the numerical procedure for solving Eq. (45) with the boundary conditions in Eqs. (51,52).

4.4 Numerical resolution procedure

The numerical solution is calculated using the determinant method, as in [15, 22]. The aim is to find the values of a control parameter for which there is a solution of Eq. (45) with mixed boundary conditions given by Eqs. (51,52). Since the growth has been considered homogeneous, the growth rates g_r and g_z can be considered as the control parameters of the elastic instability for the mucosa. The numerical procedure used to obtain these bifurcation parameters is implemented as follows. We express the solution $\boldsymbol{\eta}$ of Eq. (44), as a linear combination of three scalar functions $\boldsymbol{\eta_1}, \boldsymbol{\eta_2}, \boldsymbol{\eta_3}$, being:

$$\boldsymbol{\eta} = \nu_1 \boldsymbol{\eta_1} + \nu_2 \boldsymbol{\eta_2} + \nu_3 \boldsymbol{\eta_3} \tag{53}$$

where ν_1, ν_2, ν_3 are constant coefficients. The scalar functions $\boldsymbol{\eta}_k$, $k = \{1, 2, 3\}$, in Eq. (53) are three linearly independent copies of the solution, obtained numerically integrating the system of Eq. (45) between $r = R_0$ and $r = r_i$ and imposing three linearly independent sets $\boldsymbol{\eta_0}_k$ of initial conditions, expressed as:

$$\boldsymbol{\eta}_{0k}(r = R_0) = \{0, 0, 0, (s_{0rr})_k, (s_{0r\theta})_k, (s_{0rz})_k\}, \quad \text{with} \quad k = \{1, 2, 3\} \tag{54}$$

with arbitrary incremental stress components $(s_{0rr})_k, (s_{0r\theta})_k, (s_{0rz})_k$ at $r = R_0$. Then, we must impose that the solution in Eq. (53) satisfies the other boundary conditions in Eq. (52) at $r = r_i$, which rewrites:

$$D(g_\tau(r = r_i)) = \det \begin{pmatrix} (s_{0rr}(r_i))_1 & (s_{0r\theta}(r_i))_1 & (s_{0rz}(r_i))_1 \\ (s_{0rr}(r_i))_2 & (s_{0r\theta}(r_i))_2 & (s_{0rz}(r_i))_2 \\ (s_{0rr}(r_i))_3 & (s_{0r\theta}(r_i))_3 & (s_{0rz}(r_i))_3 \end{pmatrix} = 0 \tag{55}$$

where $(s_{0jl})_k$, $jl = \{r, \theta, z\}$, $k = \{1, 2, 3\}$ are the incremental stresses numerically calculated at $r = r_i$ from the initial value $\boldsymbol{\eta}_{0k}$. As shown in Figure 7, we calculate the bifurcation threshold $g_\tau(H)$, $\tau = \{r, z\}$ with the help of two cycles of iteration: we first iterate on the aspect ratio $H = R_0/R_i$, then, in a second cycle, we iterate on the bifurcation parameter until the stop condition in Eq. (55) is reached.

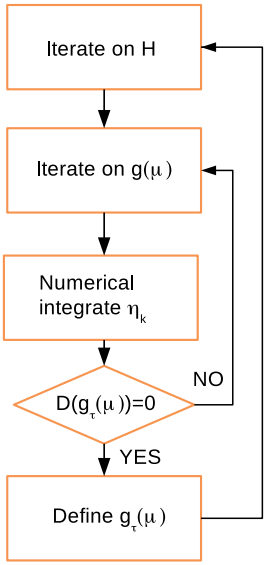

Figure 7: Implementation of the numerical scheme: after a first iteration on the aspect ratio H, it follows a second iteration on the bifurcation parameter $g(H)$. In this second cycle, the solution is numerically integrated until the condition $D((g_\tau(r = r_i))$ is satisfied and the threshold value for the parameter g_τ is obtained.

5 Results

The numerical results obtained from the linear stability analysis of the growing intestinal mucosa are presented in the following. First, we consider the mucosa as an isotropic material, with the aim to investigate the effect of the volumetric growth on the onset of instability. The volume increase is considered resulting from both isotropic ($g_r = g_z$) and anisotropic ($g_r \neq g_z$) growth processes. The curves of marginal stability depict the growth thresholds at which a bifurcation occurs in function of the aspect ratio H, and are shown for different perturbation modes. Second, the mucosa is considered as a fiber-reinforced tissue according to Eq. (7). The numerical results are shown for investigating the effect of the material anisotropy on the bifurcation thresholds for g_r and g_z, investigating the effects of the stiffness and the orientation of the reinforcing fibers on the onset of instability.

5.1 Isotropic behavior of the mucosa

Let us first consider the mucosa as an isotropic material (i.e. setting $k_1 = 0$ in Eq. (7)). The marginal stability curves obtained assuming an isotropic growth process ($g_r = g_z$) with $m = k_z$ are plotted in Figure 8 within the range of $1 < H \leq 2$. An increase of the value of the perturbation modes results

in a decrease of the growth thresholds, highlighting the occurrence of a surface instability at very short wavelengths.

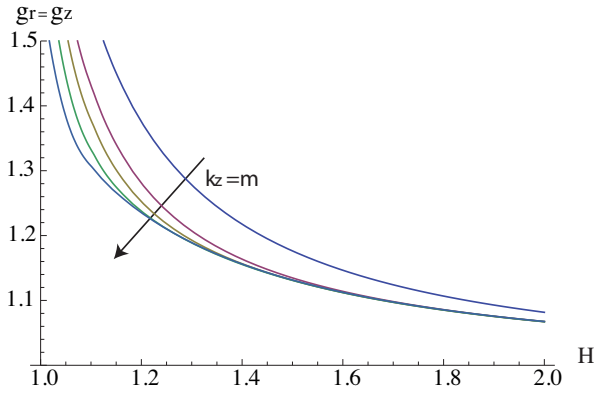

Figure 8: Marginal stability curves for isotropic growth showing the isotropic growth rate $g_r = g_z$ at different modes $k_z = m = 2, 5, 10, 15$.

The same instability mechanism occurs when considering anisotropic growth processes. The marginal stability curves are plotted in Figure 9, referring to a volume increase completely due to a radial ($g_z = 1$, left) or to a longitudinal ($g_r = 1$, right) growth process.

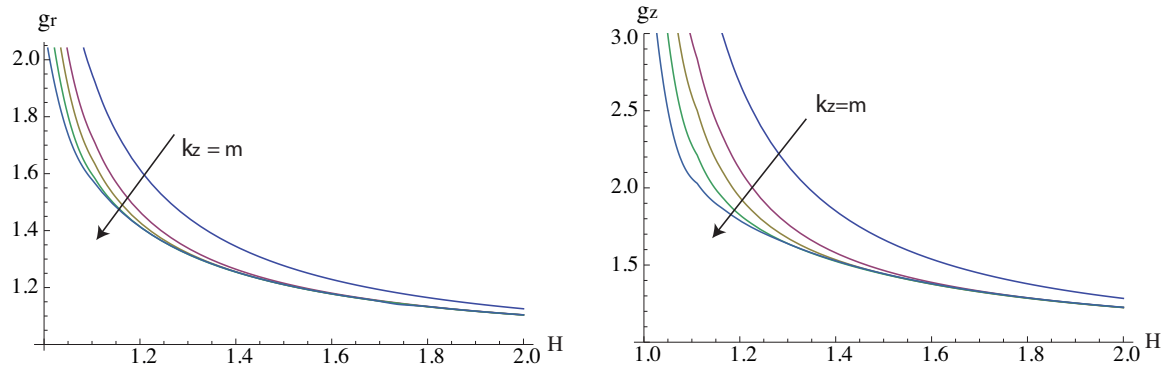

Figure 9: Marginal stability curves for anisotropic growth showing the radial growth g_r (left, setting $g_z = 1$) and the longitudinal growth g_z (right, setting $g_r = 1$) thresholds, calculated at different modes $m = k_z = 2, 5, 7, 10, 15$.

In Figure 10, the marginal stability curves are shown for different circumferential perturbation modes m, at fixed the perturbation mode in the longitudinal direction, $k_z = 10$. In the same way, fixing the circumferential perturbation mode at $m = 10$, the instability thresholds are depicted in Figure 11, for different longitudinal modes k_z.

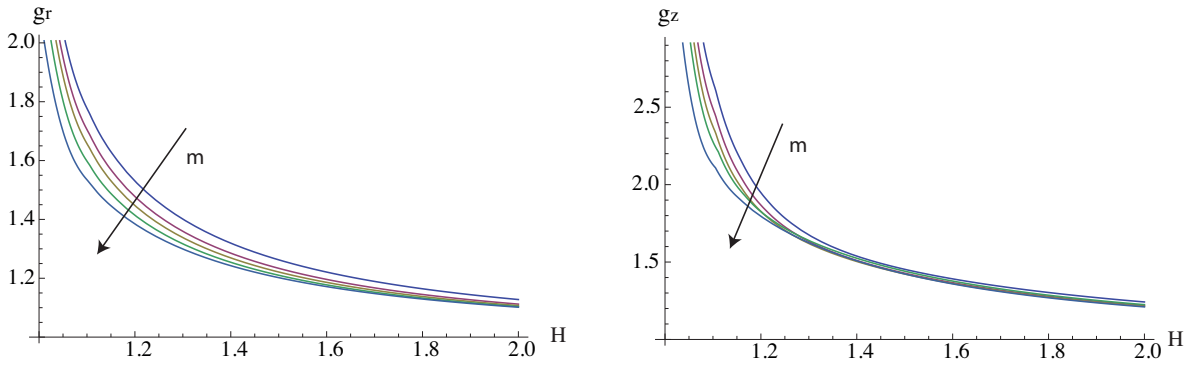

Figure 10: Marginal stability curves for anisotropic growth showing the radial growth g_r (left, setting $g_z = 1$) and the longitudinal growth g_z (right, setting $g_r = 1$) thresholds, calculated at different modes $m = 2, 5, 7, 10, 15$ and fixed $k_z = 10$.

These results confirm the occurrence of a surface instability mechanism: the growth thresholds for high values of m, k_z collapse to a single master curve in the case of thick tissues ($H > 1.5$), while a large variability on the perturbation mode appear as the aspect ratio decreases. Even if the instability is predicted for $(m, k_z) \to \infty$, we recall that the biological system will select a finite wavelength because of the existence of boundary energies penalizing the increase in the surface area of the mucosa. Although such correction of the wavelength can be calculated following the method proposed by Ben Amar and Ciarletta [23], it will be neglected in here for the sake of simplicity.

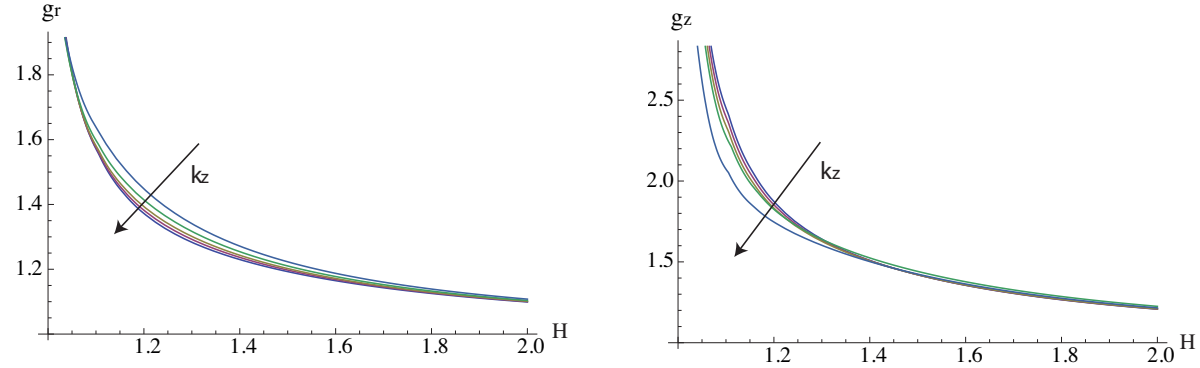

Figure 11: Marginal stability curves for anisotropic growth showing the radial growth g_r (left, setting $g_z = 1$) and the longitudinal growth g_z (right, setting $g_r = 1$) thresholds, calculated at different modes $k_z = 2, 5, 7, 10, 15$ and fixed $m = 10$.

Finally, it is useful to compare the instability thresholds for the three different growth processes investigated in terms of the total volume increase, given by $J_g = g_r^2 g_z$. In Figure 12, we depict the marginal

stability curves for J_g in the cases $g_r = g_z$, $g_r = 1$ and $g_z = 1$, predicting that the bi-dimensional surface undulations occur first when the mucosal growth is uniquely longitudinal.

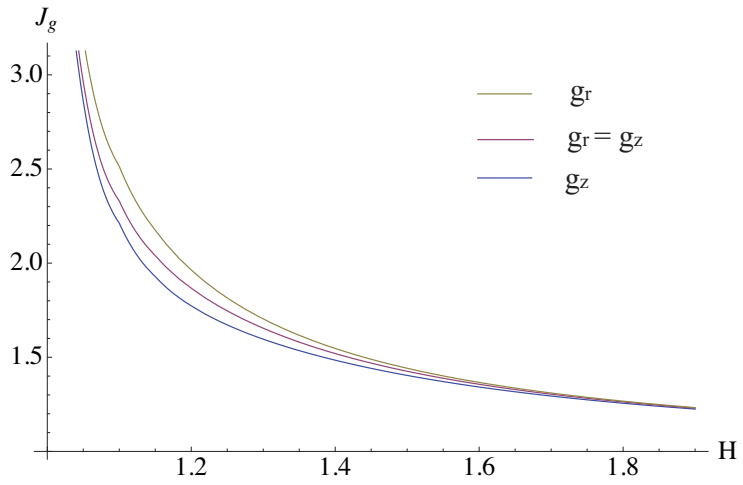

Figure 12: Marginal stability curves showing the critical volume increase J_g at modes $k_z = m = 10$ for isotropic ($g_r = g_z$, magenta) and anisotropic ($g_r = 1$, yellow and $g_z = 1$, blue) growth processes.

5.2 Anisotropic behavior of the mucosa

In this paragraph, we take into account the material anisotropy of the mucosa, and the numerical results are calculated for different cross-ply fiber angles α (Figure 13) and for different material anisotropy ratios k_1/μ, (Figure 14).

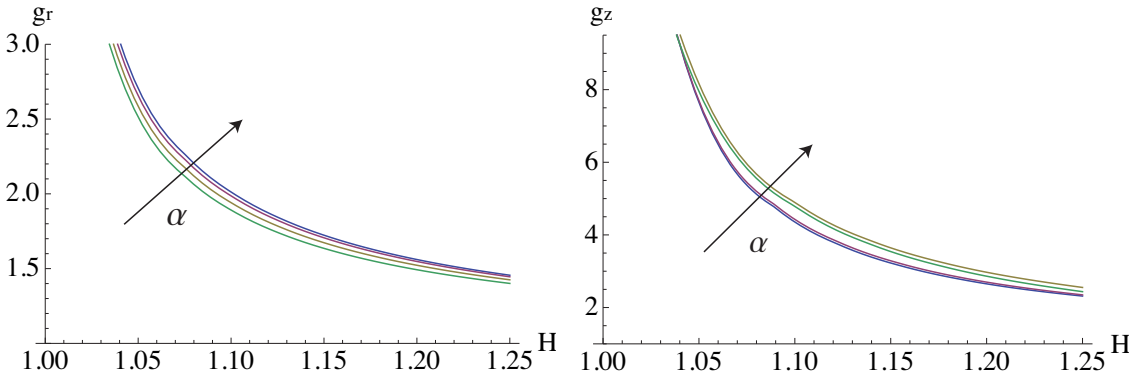

Figure 13: Marginal stability curves for anisotropic growth showing the radial growth g_r (left, setting $g_z = 1$) and the longitudinal growth g_z (right, setting $g_r = 1$) thresholds at modes $k_z = m = 5$. The material anisotropy ratio is fixed at $k_1/\mu = 10$, while the curves are shown at different cross-ply fiber angles $\alpha = (0, \pi/6, \pi/4, \pi/3)$.

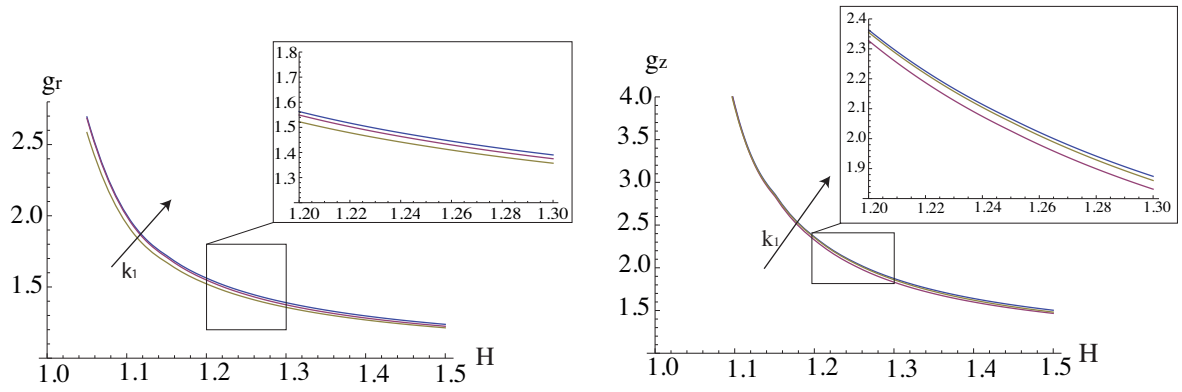

Figure 14: Marginal stability curves for anisotropic growth showing the radial growth g_r (left, setting $g_z = 1$) and the longitudinal growth g_z (right, setting $g_r = 1$) thresholds at modes $k_z = m = 5$. The cross-ply fiber angle is fixed at $\alpha = \dfrac{\pi}{4}$, while the curves are shown at different material anisotropy ratios $k_1/\mu = (0.1, 1, 10)$.

The curves plotted in Figure 13 show how increasing the cross-ply angle α the instability thresholds increase, both for the radial and longitudinal growth processes. Hence, a surface instability first occurs when the fiber orientation angle is $\alpha = 0$.

Moreover, the curves of marginal stability in Figure 14 show that the presence of a material anisotropy is a stabilizing factor, as increasing k_1/μ increases the growth thresholds of the instability. Finally, we underline that the results in Figure 13 (resp. Figure 14) are shown for $1 < H < 1.25$ (resp. 1.5) as the equation system became stiff for thicker tissues. Although other numerical techniques exist to overcome this difficulty (see [24] for a review), we preferred to avoid further complications in here, even because the mechanical effects of fiber reinforcements on instability are clearly identifiable in the observed range.

6 Discussion and conclusion

In this paper, we have proposed a morpho-elastic model of the embryonic mucosa in order to investigate the occurrence of undulated bi-dimensional patterns during the initial stages of villi morphogenesis. In Section 2, the intestinal mucosa has been modeled as a thick-walled cylinder with an outer spatial confinement. Its deformation gradient has been decomposed into a homogeneous growth component and an incompressible elastic deformation, in order to account for the spatial distribution of residual stresses arising during the constrained growth process. The mechanical behavior of the mucosa has been described using the hyperelastic model presented in Section 3. *Although similar geometrical approaches have been*

used to study the occurrence of folding instability in tubular organs [11, 12, 25], a novelty of our model is to consider the material anisotropy of the tissue. In fact, the nonlinear strain energy function includes a polyconvex energy term that depends on both the orientation and the stiffness of the collagen and elastin fibers lying under the epithelial layer. In Section 4, we have derived the equilibrium equations for the basic axial-symmetric solution of the growing mucosa and we have performed a linear stability analysis using the theory of small deformations superposed on the axial-symmetric solution. *Another novel aspect is the definition of a bi-dimensional perturbation for describing the undulated morphology at the free surface of the mucosa, as depicted in Figure 6. The resulting incremental BVP has been derived using the Stroh formulation*, and it has been solved with the help of a particular numerical scheme. The numerical results have been presented in Section 5. The growth rate thresholds for the onset of instability have been depicted in function of the aspect ratio $H = R_0/R_i$, considering isotropic and anisotropic growth processes in Figures 8 and 9, respectively. The marginal stability curves show that a short-wavelength bi-dimensional undulation occurs. An increase in the perturbation modes results in decreasing instability thresholds, showing the occurrence of a surface instability on the internal surface of the mucosal wall, as depicted in Figure 10 and Figure 11. The calculated volume increase thresholds are smaller when considering an anisotropic growth process, with the most unstable scenario being the mucosa growing only along the longitudinal direction, as shown in Figure 12. In Section 5.2, we investigated the role played by the material anisotropy of the mucosa on the onset of the surface instability. The results in Figures 13 and 14 show that an increase of both the cross-ply angle and the stiffness of the reinforcing fibers provokes an increase of the growth instability thresholds, highlighting that the material anisotropy is a stabilizing effect.

Finally, we aim at comparing the growth thresholds obtained here for the occurrence of undulated bi-dimensional patterns with those reported in [25] for prismatic deformations, representing both circumferential folding and longitudinal segmentation. This comparison shows how the instability thresholds for the bi-dimensional perturbations are smaller then those required for folding and segmentation, both for isotropic (Figure 15, left) and anisotropic (Figure 15, right) growth processes. In this way, we also prove that a bi-dimensional undulation always occurs first for a thin mucosa (i.e. H $<$ 1.15), while for thicker tubes the growth threshold is roughly the same as the one reported for circumferential folding. Using the experimental curves reported by Sbarbati [26], we have calculated the aspect ratio of the mucosa in mouse embryos within the range $H = 1.75 - 1.93$ (duodenum) and $H = 1.51 - 1.72$ (large intestine),

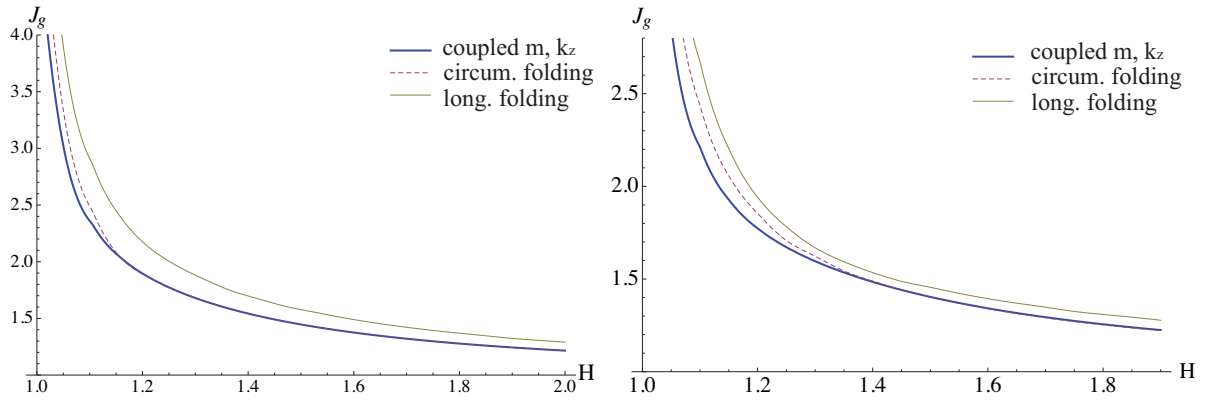

Figure 15: Instability thresholds in terms of volume increase due to isotropic (left) and anisotropic (right, $g_r = 1$) growth processes. The curves referring to the circumferential and longitudinal folding are taken from [25].

whilst the external radius is about $R_0 = 20 - 40\ \mu m$ between 12 and 16 days after incubation. The predictions of our model using such values of aspect ratio are consistent with the experimental observations of circumferential folding preceding the villi elongation mouse embryos.

Moreover, we can make a comparison of our theoretical predictions by using the experimental data of Sbarbati and Strakee [27], who reported the volume of the mouse embryonic mucosa within the period 11-19 days after incubation. Considering an initial aspect ratio Ro/Ri=1.7 from the geometrical data in [26], the critical volume increase for instability is about 1.3 according with the results sketched in Figure 15. This critical value is reached during experiments in between days 13-15, which corresponds to the period when undulated pattern are first detected, therefore validating our theoretical predictions. It is worth mentioning that even if the linear stability analysis fixes the threshold and the wavenumber of the unstable wrinkling modes, the emerging three-dimensional pattern at the tissue surface will be driven by nonlinear effects. This aspect is out of the scopes of this article, but future work will be addressed to the study of the nonlinear development of the villi morphology by minimizing the incremental strain energy inside the mucosa at orders in ε higher than two. Weakly nonlinear elastic theories [28] and numerical post-buckling techniques [29] will be used for this purpose.

In conclusion, the proposed morpho-elastic model confirms that the emergence of intestinal villi in embryos is triggered by a differential volumetric growth between the epithelial mucosa and the mesenchymal tissues. We have demonstrated that the villi morphogenesis can start directly from a bi-dimensional undulation of the mucosa or indirectly after a circumferential folding, later followed by a zig-zag pattern, as

reported by experimental observations in embryos of different species. Our theoretical analysis predicts that the selected previllous structure on the mucosa is mainly driven by the initial aspect ratio of the tubular tissue, with thinner tubes not requiring any preceding mucosal folding. The proposed morpho-elastic model highlights that both the geometrical and the mechanical properties of the mucosa strongly influence the formation of previllous structures in embryos, providing useful suggestions for interpreting the dynamics of villi morphogenesis in living organisms. *The comprehension of the interplay between growth and elasticity in the development of embryonic mucosa might also be important for understanding altered villi structures driven by pathological conditions, such as the marked flattening of the mucosal surface in coeliac disease [30].*

Acknowledgement

Partial funding by the European Community grant FP7 ERG-256605 is gratefully acknowledged.

References

[1] Rao JN, Wang JY. 2010 *Regulation of gastrointestinal mucosal growth.* San Rafael, CA: Morgan & Claypool Life Sciences.

[2] Grey RD. 1972 Morphogenesis of intestinal villi I: scanning electron microscopy of the duodenal epithelium of the developing chick embryo. *J. Morphol.* **137**, 193-214.

[3] Johnson FP. 1910 The development of the mucous membrane of the esophagus, stomach and small intestine in the human embryo. *Am. J. Anat.* **10**, 521-561.

[4] Bohórquez DV, Bohórquez NE, Ferket PR. 2011 Ultrastructural development of the small intestinal mucosa in the embryo and turkey poult: a light and electron microscopy study. *Poultry Sci.* **90**, 842-855.

[5] Burgess DR. 1975 Morphogenesis of intestinal villi II-Mechanism of formation of previllous ridges. *J. Embryol. Exp. Morphol.* **34**, 723-740.

[6] Coulombre AJ, Coulombre JL. 1958 Intestinal development I. Morphogenesis of the villi and musculature. *J. Embryol. Exp. Morphol.* **6**, 403-411.

[7] Taber LA, Humphrey JD. 2001 Stress-modulated growth, residual stress, and vascular heterogeneity. *J. Biomech. Eng.* **123**, 528-535.

[8] Gregersen H, Kassab GS, Fung YC. 2000 The zero-stress state of the gastrointestinal tract: biomechanical and functional implications. *Dig. Dis. Sci.* **45**, 2271-2281.

[9] Dou Y, Fan Y, Zhao J, Gregersen H. 2006 Longitudinal residual strain and stress-strain relationship in rat intestine. *Biomed. Eng. Online* **5**, 1-37.

[10] Li B, Cao YP, Feng XQ, Gao HJ. 2011 Surface wrinkling of mucosa induced by volumetric growth: theory, simulation and experiment. *J. Mech. Phys. Solids* **59**, 758-774.

[11] Moulton DE, Goriely A. 2011 Circumferential buckling instability of a growing cylindrical tube. *J. Mech. Phys. Solids* **59**, 525-537.

[12] Li B, Cao YP, Feng XQ. 2010 Growth and surface folding of esophageal mucosa: a biomechanical model. *J. Biomechanics* **44**, 182-188.

[13] Yang W, Fung TC, Chian KS, Chong CK. 2007 Instability of the two-layered thick-walled esophageal model under the external pressure and circular outer boundary condition. *J. Biomech.* **40**, 481-490.

[14] Hrousis CA, Wiggs BR, Drazen JM, Parks DM, Kamm RD. 2002 Mucosal folding in biologic vessels. *J. Biomech. Eng.* **124**, 334-341.

[15] Ciarletta P, Ben Amar M. 2012 Pattern formation in fiber-reinforced tubular tissues: folding and segmentation during epithelial growth. *J. Mech. Phys. Solids* **60**, 525-537.

[16] Rodriguez EK, Hoger A, McCulloch AD. 1994 Stress-dependent finite growth in soft elastic tissues. *J. Biomech.* **27**, 455-467.

[17] Holzapfel GA, Ogden RW. 2010 Constitutive modeling of arteries. *Proc. R. Soc. A* **466**, 1551-1597.

[18] Ciarletta P, Izzo I, Micera S, Tendick F. 2011 Stiffening by fiber reinforcement in soft materials: a hyperelastic theory at large strains and its application. *J. Mech. Behav. Biomed. Mater.* **4**, 1359-1368.

[19] Ogden RW. 1997 *Non linear elastic deformations.* New York: Ellis Horwood Chichester.

[20] Stroh AN. 1962 Steady state problems in anisotropic elasticity. *J. Math. Phys.* **41**, 77-103.

[21] Destrade M, Murphy JG, Ogden RW. 2010 On deforming a sector of a circular cylindrical tube into an anular tube: existence, uniqueness and stability. *Int. J. Eng. Sci.* **48**, 1212-1224.

[22] Ben Amar M, Goriely A. 2005 Growth and instability in elastic tissues. *J. Mech. Phys. Solids* **53**, 2284-2319.

[23] Ben Amar M, Ciarletta P. 2010 Swelling instability of surface-attached gels as a model of soft tissue growth under geometric constraints. *J. Mech. Phys. Solids* **58**, 935-954.

[24] Destrade M, Gilchrist MD, Prikazchikov DA, Saccomandi G. 2008 Surface Instability of Sheared Soft Tissues. *J. Biomech. Eng.* **130**, 061007.

[25] Ciarletta P, Ben Amar M. 2012 Growth instabilities and folding in tubular organs: a variational method in non-linear elasticity. *Int. J. Non-Linear Mech.* **47**, 248-257.

[26] Sbarbati R. 1982 Morphogenesis of the intestinal villi of the mouse embryo: chance and spatial necessity. *J. Anat.* **135**, 477-499.

[27] Sbarbati R, Strackee, J. 1982 A simple polynomial model of the growth of the gastro-intestinal tract in the mouse embryo. *J. Anat.* **134**, 809-815.

[28] Fu YB, Ogden, RW. 1999. Nonlinear stability analysis of prestressed elastic bodies. *Continuum Mech. Thermodyn.* **11**, 141-172.

[29] Li B, Cao YP, Feng XQ, Gao, H. 2012. Mechanics of morphological instabilities and surface wrinkling in soft materials: a review. *Soft Matter* **8**, 5728.

[30] Verbeke S, Gotteland M, Fernández M, Bremer J, Ros G, Brunser O. 2002 Basement membrane and connective tissue proteins in intestinal mucosa of patients with coeliac disease. *J. Clin. Pathol.* **55**, 440-445

Figure captions

Figure 1. Schematic structure of the intestinal wall: the inner layer called mucosa (in which concur the epithelium, the lamina propria and the muscularis mucosae), the submucosa (made of dense irregular connective tissue), the muscularis propria (oriented smooth muscles) and the outer serosa layer are evidenced.

Figure 2. Scanning electron micrographs of emerging villi in the jejunum of turkey embryos (reprinted with permission from [4]). The micrographs are taken at 21 days of incubations, and shown using scales of 100μm (a) and 10μm (b) for outlining of the morphology of the bi-dimensional undulated pattern at the free surface of the mucosa.

Figure 3. Geometrical model of the mucosa growth process: the mapping χ transforms the position $\mathbf{X}$ in the reference configuration $\mathcal{B}_0$ into the position $\mathbf{x}$ in the actual configuration $\mathcal{B}_a$.

Figure 4. The multiplicative decomposition of the deformation gradient $\mathbf{F}$: the growth component $\mathbf{F}_g$ defines a natural grown state $\mathcal{B}_g$ in which geometrical incompatibilities are allowed, and the elastic component $\mathbf{F}_e$ restores the compatibility of the tissue deformation.

Figure 5. Scheme of the deformation gradient $\mathbf{F}$ and the elastic deformation gradient $\mathbf{F}_e$, after the introduction of the incremental displacement gradient $\mathbf{\Gamma}$. The term $\dot{\mathbf{S}}_0$ represents the projection of the incremental nominal stress in the perturbed configuration $\delta\mathcal{B}_a$.

Figure 6. Morphology of the intestinal mucosa after imposing a perturbation of the axial-symmetric solution of the elastic problem, having the form of Eq. (35). The geometrical parameters are $r_0 = 2$, $r_i = 1.5$, $L = 5$, $m = 7$, $k_z = 5$ and $\epsilon = 0.15$.

Figure 7. Implementation of the numerical scheme: after a first iteration on the aspect ratio H, it follows a second iteration on the bifurcation parameter $g(H)$. In this second cycle, the solution is numerically integrated until the condition $D((g_\tau(r = r_i))$ is satisfied and the threshold value for the parameter g_τ is obtained.

Figure 8. Marginal stability curves for isotropic growth showing the isotropic growth rate $g_r = g_z$ at different modes $k_z = m = 2, 5, 10, 15$.

Figure 9. Marginal stability curves for anisotropic growth showing the radial growth g_r (left, setting $g_z = 1$) and the longitudinal growth g_z (right, setting $g_r = 1$) thresholds, calculated at different modes $m = k_z = 2, 5, 7, 10, 15$.

Figure 10. Marginal stability curves for anisotropic growth showing the radial growth g_r (left, setting $g_z = 1$) and the longitudinal growth g_z (right, setting $g_r = 1$) thresholds, calculated at different modes $m = 2, 5, 7, 10, 15$ and fixed $k_z = 10$.

Figure 11. Marginal stability curves for anisotropic growth showing the radial growth g_r (left, setting $g_z = 1$) and the longitudinal growth g_z (right, setting $g_r = 1$) thresholds, calculated at different modes $k_z = 2, 5, 7, 10, 15$ and fixed $m = 10$.

Figure 12. Marginal stability curves showing the critical volume increase J_g at modes $k_z = m = 10$ for isotropic ($g_r = g_z$, magenta) and anisotropic ($g_r = 1$, yellow and $g_z = 1$, blue) growth processes.

Figure 13. Marginal stability curves for anisotropic growth showing the radial growth g_r (left, setting $g_z = 1$) and the longitudinal growth g_z (right, setting $g_r = 1$) thresholds at modes $k_z = m = 5$. The material anisotropy ratio is fixed at $k_1/\mu = 10$, while the curves are shown at different cross-ply fiber angles $\alpha = (0, \pi/6, \pi/4, \pi/3)$.

Figure 14. Marginal stability curves for anisotropic growth showing the radial growth g_r (left, setting $g_z = 1$) and the longitudinal growth g_z (right, setting $g_r = 1$) thresholds at modes $k_z = m = 5$. The cross-ply fiber angle is fixed at $\alpha = \dfrac{\pi}{4}$, while the curves are shown at different material anisotropy ratios $k_1/\mu = (0.1, 1, 10)$.

Figure 15. Instability thresholds in terms of volume increase due to isotropic (left) and anisotropic (right, $g_r = 1$) growth processes. The curves referring to the circumferential and longitudinal folding are taken from [25].